

SMART RHESINs—Superparamagnetic Magnetite Architecture Made of Phenolic Resin Hollow Spheres Coated with Eu(III) Containing Silica Nanoparticles for Future Quantitative Magnetic Particle Imaging Applications

*Julia Feye, Jessica Matthias, Alena Fischer, David Rudolph, Jens Treptow, Radian Popescu, Jochen Franke, Annemarie L. Exarhos, Zoe A. Boekelheide, Dagmar Gerthsen, Claus Feldmann, Peter W. Roesky, and Esther S. Rösch**


Magnetic particle imaging (MPI) is a powerful and rapidly growing tomographic imaging technique that allows for the non-invasive visualization of superparamagnetic nanoparticles (NPs) in living matter. Despite its potential for a wide range of applications, the intrinsic quantitative nature of MPI has not been fully exploited in biological environments. In this study, a novel NP architecture that overcomes this limitation by maintaining a virtually unchanged effective relaxation (Brownian plus Néel) even when immobilized is presented. This superparamagnetic magnetite architecture made of phenolic resin hollow spheres coated with Eu(III) containing silica nanoparticles (SMART RHESINs) was synthesized and studied. Magnetic particle spectroscopy (MPS) measurements confirm their suitability for potential MPI applications. Photobleaching studies show an unexpected photodynamic due to the fluorescence emission peak of the europium ion in combination with the phenol formaldehyde resin (PFR). Cell metabolic activity and proliferation behavior are not affected. Colocalization experiments reveal the distinct accumulation of SMART RHESINs near the Golgi apparatus. Overall, SMART RHESINs show superparamagnetic behavior and special luminescent properties without acute cytotoxicity, making them suitable for bimodal imaging probes for medical use like cancer diagnosis and treatment. SMART RHESINs have the potential to enable quantitative MPS and MPI measurements both in mobile and immobilized environments.

1. Introduction

The introduction of magnetic particle imaging (MPI)^[1,2] in 2001 at Philips Research Laboratory marked the beginning of the development of a new tomographic medical diagnostic device with high spatial ($\approx 500 \mu\text{m}$) and temporal resolution (up to 21 ms^[3]), outstanding contrast, and high sensitivity ($\approx 10^{-6} \text{ M}$).^[4] MPI as ionizing-radiation-free imaging technology uses oscillating magnetic fields (in the range of tenth of kHz) for signal excitation and a (quasi-) static magnetic gradient field for spatial encoding to allow background-free, signal attenuation-free tomographic visualization of deep body regions using superparamagnetic^[5] nanoparticle (NP) tracers and has been proven to allow for a vast variety of biomedical applications.^[4,6,7a,b] The commercially available synomag and perimag (micromod, Germany) are the most commonly used MPI tracers nowadays due to their better signal-to-noise ratio and availability compared to Resovist

J. Feye, E. S. Rösch
Faculty of Engineering
Baden-Württemberg Cooperative State University Karlsruhe
76133 Karlsruhe, Germany
E-mail: esther.roesch@dhbw-karlsruhe.de

J. Feye, D. Rudolph, J. Treptow, C. Feldmann, P. W. Roesky
Institute of Inorganic Chemistry
Karlsruhe Institute of Technology
76131 Karlsruhe, Germany

 The ORCID identification number(s) for the author(s) of this article can be found under <https://doi.org/10.1002/sml.202301997>.

© 2023 The Authors. Small published by Wiley-VCH GmbH. This is an open access article under the terms of the Creative Commons Attribution-NonCommercial-NoDerivs License, which permits use and distribution in any medium, provided the original work is properly cited, the use is non-commercial and no modifications or adaptations are made.

J. Matthias, A. Fischer
Department of Optical Nanoscopy
Max Planck Institute for Medical Research
69120 Heidelberg, Germany

R. Popescu, D. Gerthsen
Laboratory for Electron Microscopy
Karlsruhe Institute of Technology
76131 Karlsruhe, Germany

J. Franke
Bruker
BioSpin MRI GmbH
Preclinical Imaging Division
76275 Ettlingen, Germany

A. L. Exarhos, Z. A. Boekelheide
Department of Physics
Lafayette College
Easton, PA 18042, USA

DOI: 10.1002/sml.202301997

(Bayer Healthcare, Germany).^[8] The subject of current research is the development of suitable MPI tracers.^[9] An important feature of the MPI technique is the direct quantification of the spatial distribution of the signal.^[4] The magnetic NP (MNP) signal scales with the amount of MNPs per voxel, which makes MPI an attractive option for quantitative imaging.^[2] It has been shown mathematically and experimentally that the detected signal intensity is linearly proportional to the sum of non-interacting tracer particles in a voxel.^[10] However, particles can be altered under physiological conditions, for example, by aggregation or opsonization.^[11,12] The linear relationship of the signal to the iron concentration then becomes non-linear, which hinders the accurate quantification of the magnetization and iron content at a particular tissue site.^[12,13] Nevertheless, non-linear effects can provide valuable information. For example, these signals have already been used to reconstruct temperature and viscosity.^[14] However, our goal is to enable quantitative measurements using the particle architecture presented herein.

The Brownian relaxation (physical rotation of the particle core) and the Néel relaxation (rotation of the magnetization vector of the particle) are decisive for the signal intensities.^[15] Most MPI NPs described in the literature so far are characterized by strong interactions or bonds of firmly interconnected core/shell structures.^[16–18] The orientation of the magnetic moment is related to both types of relaxation, and these depend on each other in core/shell structures due to the strong interaction forces between core and shell. In addition to the classical core/shell NPs,^[19,20] other types of NPs with sophisticated particle architectures have been reported.^[21–23] Recently, novel types of NP structures for MPI application have been presented, however, iron oxide NPs were incorporated into soft shells such as liposomes, micelles or placed on the surface of poly(lactic-co-glycolic acid) microspheres.^[24–27] It could be shown that micelle-based iron oxide microspheres significantly increased the magnetic particle spectroscopy (MPS) signal in comparison to commercial Resovist.^[24] However, microspheres are too large for many therapeutic drug delivery purposes. Liposomes are prone to lymph node uptake, interactions with native lipoproteins in the bloodstream,^[28] or thermal disruption and are further known for their poor encapsulation ability.^[29]

Hollow nanospheres with a covalently cross-linked polymer shell were synthesized to make the magnetic NPs inside the cavity of the nanosphere less dependent on its external shell (yolk/shell NPs), since the magnetic moment of MPI-suitable NPs depends on both Néel and Brownian relaxation, which are independent of each other, but the latter is affected by environmental changes such as viscosity and rotational mobility of the NPs.^[22] To achieve this, hollow nanospheres (shell) filled with superparamagnetic NPs (yolk) have been used.^[30–33] The hollow nanospheres make it possible to gain a basic understanding of the properties of the MPI signal generation even under physiological conditions, as the MNPs inside can contribute to the MPI signal generation unaffected by the external environment. Our hypothesis is that the magnetic characteristics detected in MPS will persist during MPI, despite any alterations to the outer shell caused by physiological conditions, owing to the controlled environment within the hollow sphere. This would allow the targeted investigation of the MPI image formation and the exploitation of the quantification potential of the MPI modality regardless of the nanosphere microenvironment.

Polymer shells, for example, such as phenolic formaldehyde resins (PFR) can enclose drugs or NPs.^[34,35] The roots of the respective polymer chemistry can be traced back to Baekeland's patent of 1909, which describes the reaction of phenol and formaldehyde to form insoluble products.^[36] Phenol can polymerize with an excess of formaldehyde under basic conditions to form a resol resin.^[37] Since phenol is relatively slow-reacting,^[38] more reactive monomers such as 2,4-dihydroxybenzoic acid (DA) or resorcinol are often used.^[39–43] The respective products are then referred to as PFR.

Solid PFR nanospheres are easy to prepare, biocompatible and known for their good intrinsic fluorescence properties, making them suitable for potential applications in bioimaging.^[44–46] However, the luminescence intensity of PFR is weak compared to bright luminescent dyes specialized for bioimaging methods.^[44] It can be enhanced by coating the surface with an additional luminophore such as CdTe-Qdots.^[45] Nonetheless, cadmium-containing luminophores are prone to the liberation of free Cd²⁺, thus being highly cytotoxic.^[47]

Hollow PFR nanospheres (PFRH) can enclose MNPs, which make them easy to purify and attractive candidates for biomedical applications such as MPI, magnetic resonance imaging (MRI), and magnetic fluid hyperthermia (MFH).^[34a,b] Due to the presence of carboxylic acid and phenolic OH groups, the outer side of the polymer shell can be further modified with luminophores, molecules for targeted delivery or molecules for general chemical reactions. The PFRH particle architecture, with its various potential functionalizations, holds great promise for theranostic applications, such as the combination of MPI and MFH. NPs for biological and biomedical applications commonly combine different modalities such as magnetism and luminescence,^[16,29,48] rendering the particles suitable for *in vitro* fluorescence microscopy or *in vivo* applications such as hyperthermia,^[49] theranostics,^[50] drug targeting, and imaging.^[51,52] Although luminescence functionalization is challenging to achieve chemically, it is also vulnerable to attenuation when used in tissue situated deep within the body.

In addition to chemical stability during synthesis, several optical properties are critical to a successful application, such as a high quantum yield, high photostability, the absence of quenching, and absorption and emission wavelengths that suit the respective equipment.^[53] There are different types of luminophores, for example, organic dyes, quantum dots or trivalent rare-earth probes.^[53,54] In comparison to quantum dots and trivalent rare-earth probes, classical organic dyes, such as fluoresceins, rhodamines and most cyanines, bleach faster, and display shorter emission lifetimes, rather lower extinction coefficients, a tendency to pH dependence, and self-quenching at high concentrations.^[55–57] Quantum dots are very popular because of their remarkable optical properties,^[58] but are challenging to functionalize due to irreversible precipitation and quenching phenomena.^[59–62] Luminescent lanthanide(III) (Ln^{III}) ion complexes, in particular Eu(III) complexes, provide a promising alternative to organic dyes and quantum dots in terms of thermodynamic stability and brightness.^[54] Eu(III) complexes containing thenoyltrifluoroacetone (TTA) such as Eu(TTA)₃ are well known for their characteristic red emission upon ultraviolet (UV) excitation, their long luminescent lifetimes and their decent quantum yields depending on their respective ligands in solution (e.g., $\Phi([\text{Eu}(\text{TTA})_3(\text{H}_2\text{O})_2] \text{ in } \text{CHCl}_3) = 0.09$,

$\Phi([\text{Eu}(\text{TTA})_3(\text{DBSO})_2] \text{ in } \text{CHCl}_3) = 0.27$ (DBSO: dibenzylsulfide).^[63] The large Stokes shift of $\text{Eu}(\text{TTA})_3$ complexes allows the distinct separation of excitation and emission bands. Additionally, their red emission facilitates the easy delineation from any autofluorescence signal.^[64] The excitation of the lumiphore with high energy wavelengths in the UV region can be circumvented by using two-photon excitation,^[65,66] making the complexes suitable candidates for biological cell probes.^[67]

As the luminescence of $\text{Eu}(\text{III})$ ions is quenched by non-radiative energy transfer through OH vibrations of water molecules,^[68,69] $\text{Eu}(\text{III})$ ion leakage must be prevented by ensuring $\text{Eu}(\text{III})$ complex stability under physiological conditions to allow for bright emission.^[54] When used for luminescence functionalization of NPs for biological applications, $\text{Eu}(\text{III})$ complexes are mainly combined with core/shell NPs.^[70] To date, only a few examples of luminescent and magnetic hollow nanospheres have been reported, and the synthesis of empty or non-magnetic metal-filled PFR hollow nanospheres has mainly been established for nanosized hollow carbon spheres (HCS), which cannot be functionalized further.^[34,35,42,71] However, the installation of variable functional groups on the outer polymer shell offers unprecedented opportunities for further (bio-)chemical modification, including luminescence functionalization, and organelle and tissue targeting.^[72–74] Filled hollow nanospheres, also referred to as yolk/shell NPs or nanorattles, open up new possibilities for functionalization so far out of reach with classical core/shell NPs for theranostic and quantitative MPI applications.^[25,75–79] This superparamagnetic magnetite architecture made of phenolic resin hollow spheres coated with $\text{Eu}(\text{III})$ containing silica nanoparticles, herein named SMART RHESINs, was synthesized and studied.

2. Results and Discussion

2.1. Synthesis and Characterization of SMART RHESINs

In the first step, we synthesized oleate-coated magnetite NPs. Many approaches are known for the synthesis of nanosized magnetite, such as co-precipitation, hydrothermal, solvothermal, thermal decomposition, microemulsions, and sol-gel.^[29,80,81] **Figure 1** schematically depicts the synthesis route followed in this study to produce SMART RHESINs. We chose the microwave-assisted solvothermal synthesis route,^[82] starting with iron(III) oleate, because it is a fairly simple method for obtaining oleate-coated magnetite NPs ($\text{Fe}_3\text{O}_4@oleate$) with narrow size distribution and high crystallinity. In the second step, the magnetite surface was modified by a ligand exchange process with sodium hydroxide yielding water-dispersible superparamagnetic magnetite NPs ($\text{Fe}_3\text{O}_4(aq)$).^[83,84] In the third step, the magnetite NPs were encapsulated in poly(ethylene oxide)-poly(propylene oxide)-poly(ethylene oxide) block co-polymer Pluronic P123 ($\text{EO}_{20}\text{PO}_{70}\text{EO}_{20}$) and sodium oleate, which formed mixed micelles^[71] by hydrophobic interactions,^[34] using the soft-template process to generate hollow nanostructures. Subsequently, the polymer shell was formed on the surface of the micelles through weak acid-base interactions by heating after adding 2,4-dihydroxybenzoic acid and hexamethylenetetramine (HMT),^[35] yielding $\text{Fe}_3\text{O}_4(aq)@PFRH$.

The question of whether the micelle-forming substances P123 and sodium oleate (SO) are still present in the hollow sphere or whether they can be washed out cannot be answered simply. While in the original publications,^[34,35] the hollow spheres were thermally treated at high temperatures (pyrolysis between 400 and 650 °C) to form HCS, thus carbonizing any organic compounds, this step was not performed in our synthesis route to preserve the functional groups. We hypothesize that the polymer P123 and sodium oleate cannot be easily washed out, so we draw them graphically in our schematic illustration of the reaction model of the synthesis route (Figure 1e,h). The size of the hollow nanostructures was measured with dynamic light scattering (DLS) and transmission electron microscopy (TEM) and their diameter ranged from ≈ 150 to ≈ 300 nm, and their shell thickness from ≈ 10 to ≈ 30 nm. The outer surface of the polymer shell was covered with a sufficiently large number of accessible carboxylic acid groups for further chemical reactions.

To prevent leakage and quenching of $\text{Eu}(\text{III})$ ions, the $\text{Eu}(\text{III})$ complex was incorporated into silica NPs using the modified Stöber method.^[53] In the first attempt, the luminescent silica NPs were encapsulated in the nanosphere along with the magnetite NPs to keep the outer shell clear for mono-functionalization. However, the luminescence was quenched after several minutes during micellization before polymerization could be carried out. Instead, we modified the surface of the $\text{Eu}(\text{III})$ complex containing silica NPs with (3-aminopropyl)triethoxysilane (APTES) to obtain amino-functionalized Eu-TTA-Si NPs. To yield SMART RHESINs, the amino-functionalized luminescent silica NPs were then coupled to the outside of the $\text{Fe}_3\text{O}_4(aq)@PFRH$ nanosphere via the carboxylic acid groups using *N,N*-diisopropylcarbodiimide (DIC) and hydroxybenzotriazole (HOBt) in acetonitrile.^[85]

The morphology and lattice structure of hydrophilic magnetite NPs, Eu-TTA-Si NPs, $\text{Fe}_3\text{O}_4(aq)@PFRH$ nanospheres, and SMART RHESINs were examined by TEM and scanning (S)TEM (**Figure 2**). TEM overview images and high-resolution (HR)TEM images show highly uniform $\text{Fe}_3\text{O}_4(aq)$ NPs in terms of both particle size and particle shape (Figure 2a–c). Presence and purity of the $\text{Fe}_3\text{O}_4(aq)$ NPs were further validated by X-ray powder diffraction analysis (Figure S1, Supporting Information). Moreover, HRTEM images indicate locally ordered atom configurations with lattice fringes extending through whole $\text{Fe}_3\text{O}_4(aq)$ NPs, which supports their monocrystalline structure. The whole NP shown in Figure 2c is a single Fe_3O_4 (magnetite) monocrystal with a cubic structure as indicated by the good agreement between its 2D Fourier transform and the calculated diffraction pattern of bulk cubic Fe_3O_4 (space group Fd-3m, space group number 227) with $a = 8.3941$ Å in the [215]-zone axis (Figure 2d).^[86] A high-angle annular dark-field (HAADF)-STEM overview image of Eu-TTA-Si NPs and corresponding element maps obtained by energy-dispersive X-ray spectroscopy (EDXS) area scans show particle agglomerations as well as the presence of Si and Eu (Figure 2e–h). Particle agglomeration likely occurred during the preparation (drying) of colloidal stable suspensions for TEM investigation. HAADF-STEM imaging confirms the yolk/shell structure of typical $\text{Fe}_3\text{O}_4(aq)@PFRH$ nanospheres and of SMART RHESINs both containing a large number of small hydrophilic

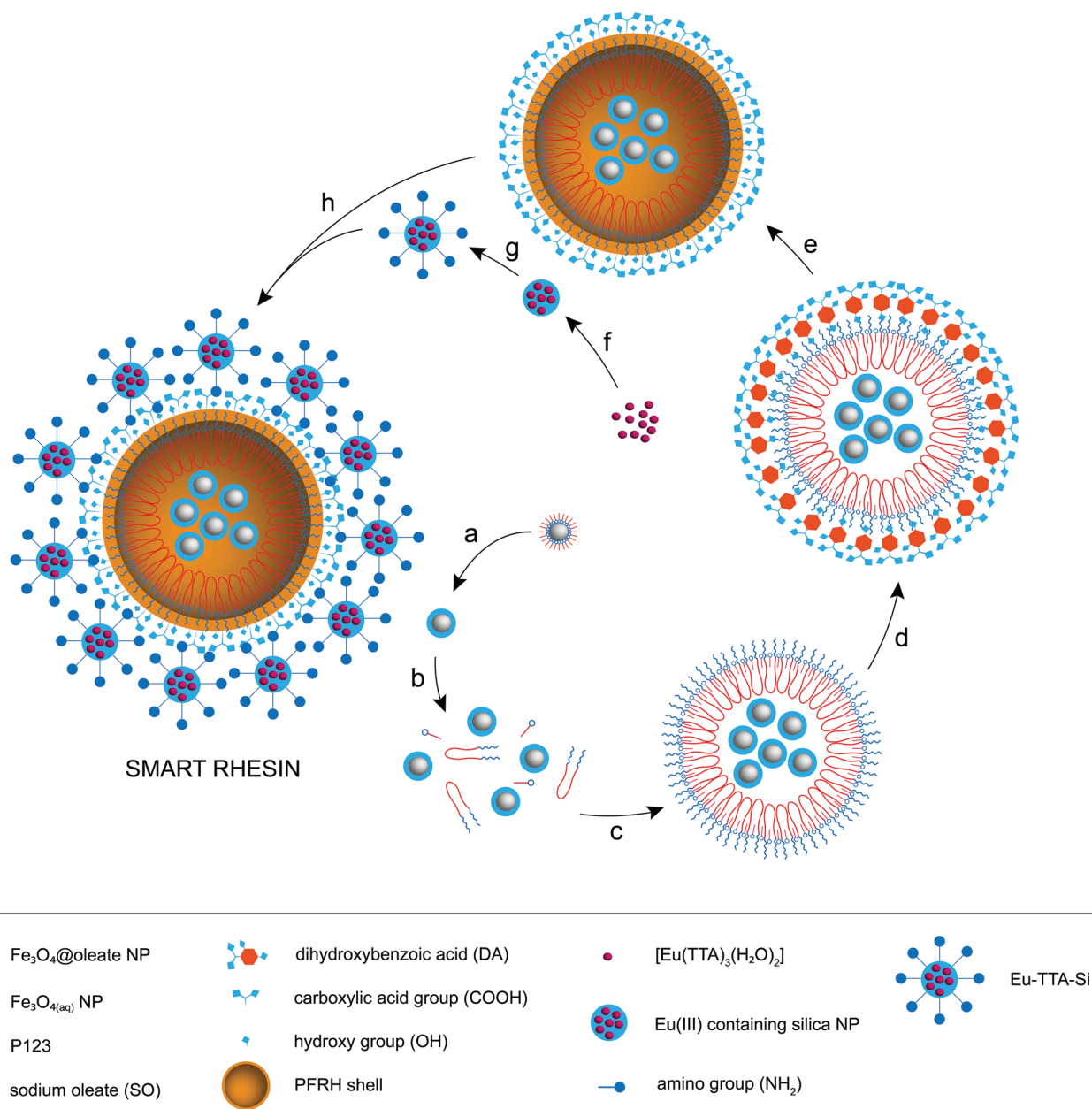


Figure 1. Schematic illustration of the reaction model for the synthesis route of SMART RHESINs. a) Ligand exchange of oleate-coated Fe₃O₄ NPs, b) solution of P123, SO and Fe₃O_{4(aq)} NPs, c) micelle formation, d) added polymer precursors to form emulsion droplets, e) hydrothermal process, f) Eu(III) complex containing silica NPs, g) NH₂-modification of silica surface, h) peptide coupling of luminescent Eu-TTA-Si NPs with COOH-groups of outer PFRH shell.

magnetite NPs. HAADF-STEM imaging yields mass-thickness contrast with dominant Z (atomic number) contrast at comparable TEM-sample thicknesses. The Fe₃O_{4(aq)}@PFRH nanosphere shows a shell with low intensity as expected for the organic weakly scattering shell material (Figure 2i) and confirmed by the carbon map (Figure 2k). The high intensity in the nanosphere interior indicates a large number of Fe₃O₄ NPs with a size of 5 to 10 nm and is also visualized by the Fe distribution (Figure 2j). The Fe₃O_{4(aq)}@PFRH nanosphere is not completely filled with Fe₃O₄ NPs but also contains a dark region that is associated with a hollow region (Figure 2j,i). The

structure of the SMART RHESIN is similar. The nanosphere interior is partially filled with Fe₃O₄ nanoparticles (Figure 2m and Fe distribution Figure 2n). The HAADF-STEM intensity of the SMART RHESIN nanosphere shell is comparably high due to the strongly scattering Eu atoms (Figure 2m and Eu distribution in Figure 2o). Particle size and size distribution of oleate-coated Fe₃O₄ NPs, micelle solution, Fe₃O_{4(aq)}@PFRH nanospheres and SMART RHESINs were determined by DLS (Figure S2, Supporting Information) and all relevant Fourier transform infrared (FT-IR) spectra of the precursors and the synthesized particles are in good agreement with the literature

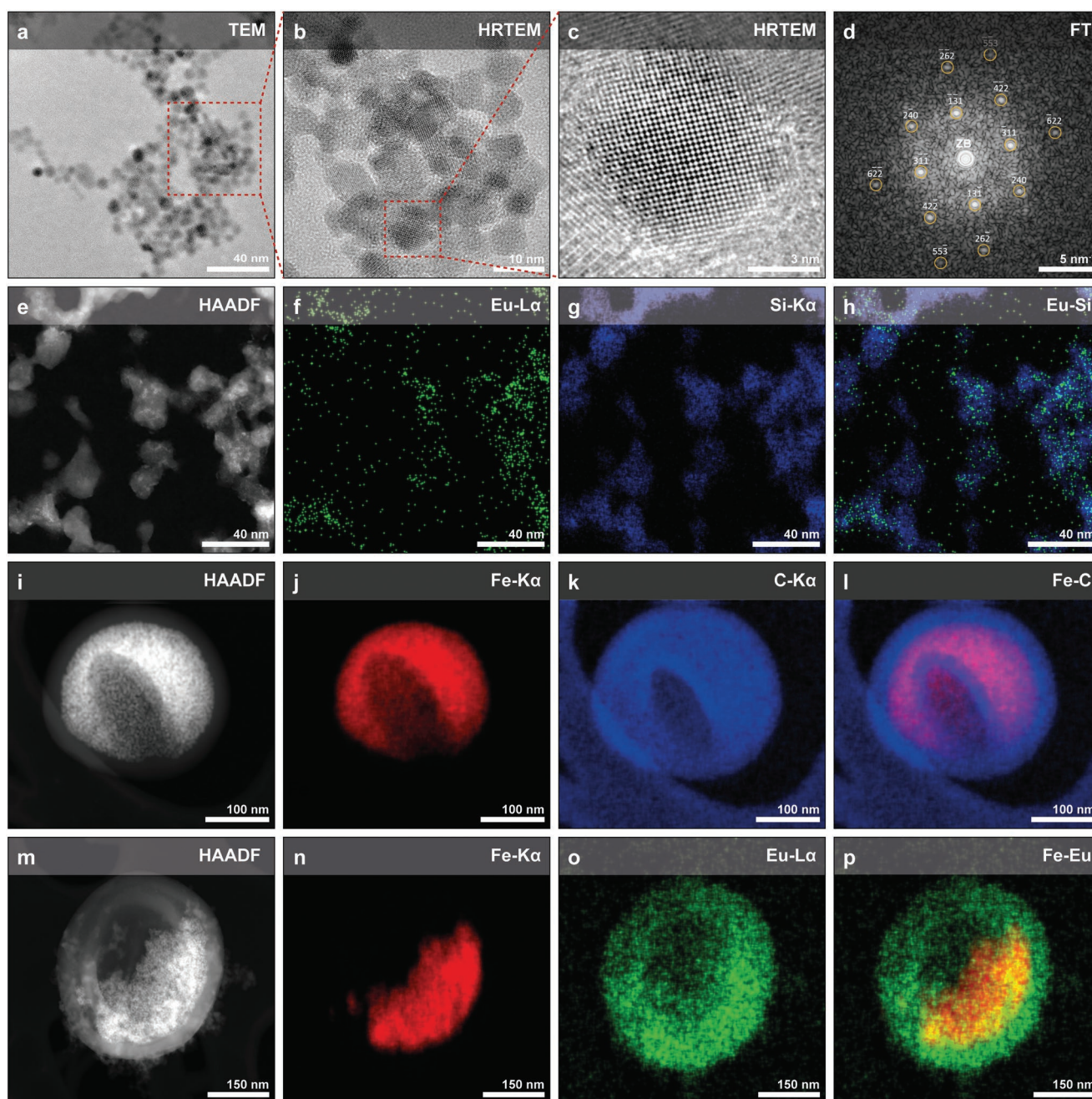


Figure 2. (S)TEM analysis of SMART RHESINs with a) TEM overview image of $\text{Fe}_3\text{O}_4(\text{aq})$ NPs, b) HRTEM image of small crystalline $\text{Fe}_3\text{O}_4(\text{aq})$ NPs, c) HRTEM image of one single $\text{Fe}_3\text{O}_4(\text{aq})$ nanoparticle with cubic lattice structure and extended lattice fringes throughout whole nanoparticle supporting its monocrystalline structure, and d) corresponding 2D Fourier transform of (c) with calculated diffraction pattern for cubic $\text{Fe}_3\text{O}_4(\text{ag})$ with space group Fd-3m, space group number 227 and $a = 8.3941 \text{ \AA}$ in the [215]-zone axis, e) HAADF-STEM overview image of Eu-TTA-Si NPs and the distributions of f) Eu, g) Si, and h) Eu and Si obtained by an Energy Dispersive X-Ray Spectroscopy (EDXS) area scan, i) HAADF-STEM image of a single $\text{Fe}_3\text{O}_4(\text{aq})$ @PFRH nanosphere and distributions of j) Fe, k) C, and l) Fe and C. m) HAADF-STEM image of one SMART RHESIN particle and distributions of n) Fe, o) Eu, and p) Fe and Eu.

(Figures S10–S17, Supporting Information).^[34,87–89] To determine whether or not the Eu-TTA-Si NPs are covalently bound to the surface of the PFRH shell, we recorded IR spectra of a mixture of Eu-TTA-Si NPs and $\text{Fe}_3\text{O}_4(\text{aq})$ @PFRH nanospheres (Eu-TTA-Si NPs not covalently bound to PFRH, Figure S17, Supporting Information) and compared them with the FT-IR spectra of

SMART RHESINs (Figures S16 and S17, Supporting Information). It is inconclusive from the data whether the Eu-TTA-Si NPs are covalently bound to the surface or not, even though we assume that they are, since the luminescence functionalization cannot be removed from the surface even by extensive washing with solvent.

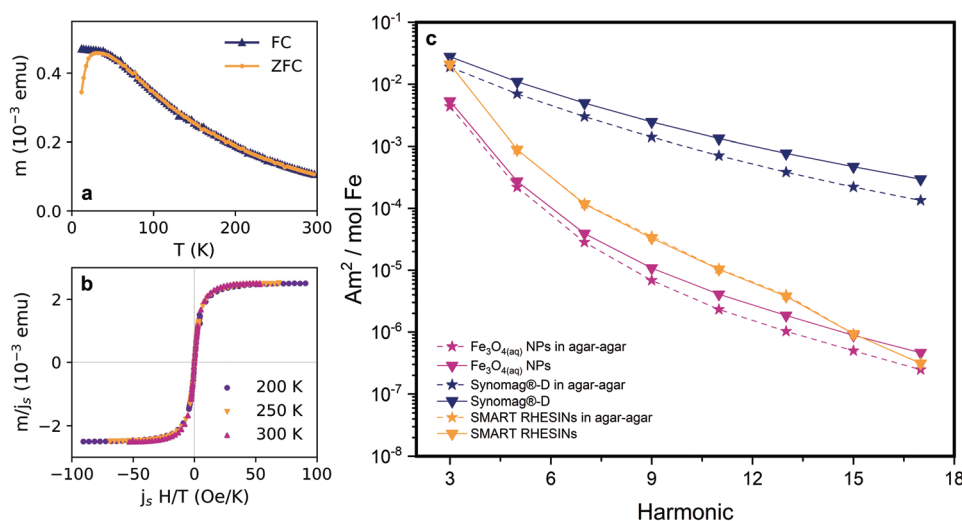


Figure 3. Magnetic behavior of SMART RHESINs. For a sample of dried SMART RHESINs, a) the magnetic moment (m) as a function of temperature (T), measured with an applied field (H) of 100 Oe. Data was measured upon warming, after first cooling in either zero field (ZFC) or in a field of 100 Oe (FC). b) m as a function of H/T . Here, both m and H/T are scaled by $j_s = m_s(T)/m_s(10\text{ K})$ to account for the temperature-dependence of the spontaneous magnetization. c) MPS spectrum of $\text{Fe}_3\text{O}_4(\text{aq})$ NPs (magenta) and SMART RHESINs (yellow) in deionized water (solid lines) and in 10 mg mL^{-1} agar-agar solution (dashed lines) at 20 mT drive field excitation at 25.25 kHz. For better comparison, the commonly used MPI tracer synomag-D (dark blue) was also measured in water and in agar-agar solution and the spectra have been normalized to the iron concentration of the individual samples.

2.2. Magnetic Behavior of SMART RHESINs

2.2.1. Superparamagnetism

For potential MPI application, superparamagnetic behavior is a prerequisite. Measurements of the direct current (DC) magnetic moment (m) as a function of temperature (T) and applied field (H) confirm the superparamagnetic behavior of the SMART RHESINs. Measurements of m versus T under ZFC and field cooled (FC) conditions (Figure 3a) show a blocking temperature, T_B , of 31 K, as estimated from the peak in the ZFC curve. Measurements of m versus H were made at $T > T_B$ (200, 250, and 300 K) and show zero coercivity within the limits of the apparatus. To further confirm superparamagnetic behavior, in Figure 3b we show m versus H/T for the three temperatures; the strong overlap of the data indicates superparamagnetism.^[90a,b] The $\text{Fe}_3\text{O}_4@\text{PFRH}$ NPs show very similar superparamagnetic behavior, with a blocking temperature of 28 K and good overlap of m versus H/T at $T > T_B$ (see Figure S3, Supporting Information), indicating that the magnetic behavior does not appear to be affected by the modification of the polymer shell. Further details regarding the measurement and analysis of the magnetic moment can be found in Section S4.2.9, Supporting Information.

2.2.2. Magnetic Particle Spectroscopy Analysis

To investigate the alternating current (AC) magnetic properties of the $\text{Fe}_3\text{O}_4(\text{aq})$ NPs and the SMART RHESINs in more detail, we performed MPS measurements (MPS-3, Bruker BioSpin MRI GmbH, Germany) in different dispersion media (agar-agar vs deionized water). MPS measures the magnetic response of MNPs

to an oscillating magnetic field. The change of the particle's magnetization is measured as induced voltage in a receive coil, in our case at 25.25 kHz and excitation amplitude at 20 mT. Because of the NP's non-linear magnetization behavior, the induced particle signal contains despite the fundamental frequency also harmonics thereof. The particle MPS spectrum indicates the particle's performance as MPI tracer. Samples were mixed with agar-agar (immobilized samples) or deionized water (mobile samples) and the measured spectra were normalized to the iron concentration of the different samples. The performance of the $\text{Fe}_3\text{O}_4(\text{aq})$ NPs and the SMART RHESINs is shown in Figure 3c. synomag-D ($d_{\text{DLS}} = 70\text{ nm}$, micromod, Germany) was used as a standard, since it is a commonly used MPI tracer. To evaluate the performance of the samples regardless of their iron content, we analyzed different concentration ratios and plotted the respective slopes of the calibration line for all samples based on the odd harmonics (see Figure S4, Supporting Information). The synomag-D NPs show the best performance, as expected from a high-performance tracer for MPI applications. The spectral amplitudes for the $\text{Fe}_3\text{O}_4(\text{aq})$ NPs and SMART RHESINs continuously decrease, reaching a signal value of $4.6 \times 10^{-7}\text{ Am}^2\text{ mol}^{-1}\text{ Fe}$ for the $\text{Fe}_3\text{O}_4(\text{aq})$ NPs and $3.1 \times 10^{-7}\text{ Am}^2\text{ mol}^{-1}\text{ Fe}$ for the SMART RHESINs at the 17th harmonic. For all immobilized samples, the amplitudes are significantly lower than for the corresponding liquid ones, except for the SMART RHESINs, for which the signals overlap (Figure 3c, yellow lines). This can be explained by not inhibiting the Brownian rotation of the SMART RHESINs—fostering our hypothesis—compared to immobilized $\text{Fe}_3\text{O}_4(\text{aq})$ and the synomag-D NPs, which limits the dynamic response of the NPs to an external oscillating magnetic field.^[91] Through our findings, we have been able to validate our hypothesis and present a novel methodology for quantifying the magnetization response of NPs in MPS and potential MPI measurements, regardless of the mobility status of the NPs.

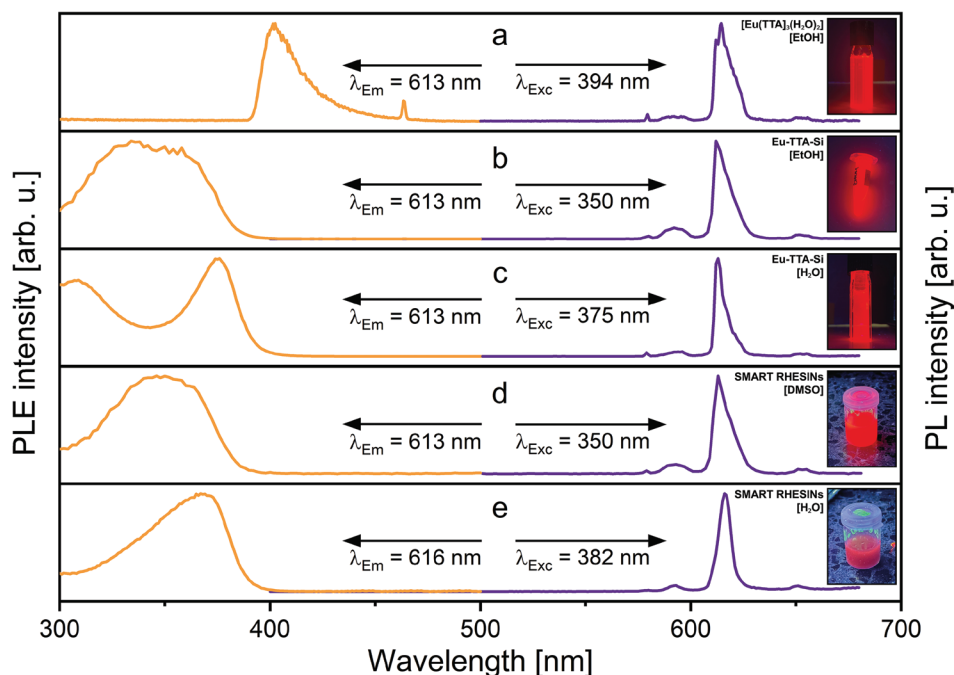


Figure 4. Photoluminescence emission (PL) and excitation (PLE) spectra of a) native and b,c) silica-functionalized $[\text{Eu}(\text{TTA})_3(\text{H}_2\text{O})_2]$ complex in (b) EtOH and (c) H_2O as well as of d,e) SMART RHESINs in (d) DMSO and (e) H_2O . The PL emission and the PLE spectra were recorded at the indicated wavelengths and normalized. The pictures show the samples under UV lamp illumination (365 nm) (compare Movie S4, Supporting Information: magnetic and luminescent properties of SMART RHESINs in H_2O excited at 365 nm).

2.3. Photoluminescence Properties of SMART RHESINs

To characterize the photoluminescent properties of the bimodal hollow nanospheres, photoluminescence emission (PL) and photoluminescence excitation (PLE) spectra of the $[\text{Eu}(\text{TTA})_3(\text{H}_2\text{O})_2]$ complex in ethanol (EtOH) (Figure 4a), the Eu-TTA-Si NPs in ethanol (Figure 4b) and deionized H_2O (Figure 4c), and SMART RHESINs in dimethyl sulfoxide (DMSO) (Figure 4d) and deionized H_2O (Figure 4e) were recorded at room temperature.

The PLE spectrum of the $[\text{Eu}(\text{TTA})_3(\text{H}_2\text{O})_2]$ complex displays an absorption band peaking at 394 nm, covering the spectral range from 390 to 475 nm, for which the peaks assigned to the ${}^7\text{F}_0 \rightarrow {}^5\text{L}_6$ (394 nm) and ${}^5\text{D}_2 \rightarrow {}^7\text{F}_0$ (465 nm) transitions of the trivalent europium ion (Figure 4a) are in good agreement with the literature.^[53] Both PLE spectra of the Eu-TTA-Si NPs (Figure 4b,c) as well as both PLE spectra of SMART RHESINs (Figure 4d,e) show a broad absorption band in the 300 to 400 nm range, with a PLE onset at around 400 nm, which is attributed to the $\text{S}_0 \rightarrow \text{S}_1$ allowed transition in the TTA ligands. The PLE profile difference between the native $[\text{Eu}(\text{TTA})_3(\text{H}_2\text{O})_2]$ complex and the Eu-TTA-Si NPs as well as SMART RHESINs suggest effective interactions both between the $[\text{Eu}(\text{TTA})_3(\text{H}_2\text{O})_2]$ complex and the silica network and likewise between the Eu-TTA-Si NPs and SMART RHESINs. In all individual PL spectra, the absence of a broad band between 450 and 600 nm, which would correspond to the triplet state excitation of the TTA ligand, indicates an efficient ligand-to-metal energy transfer (Figure 4a–e).

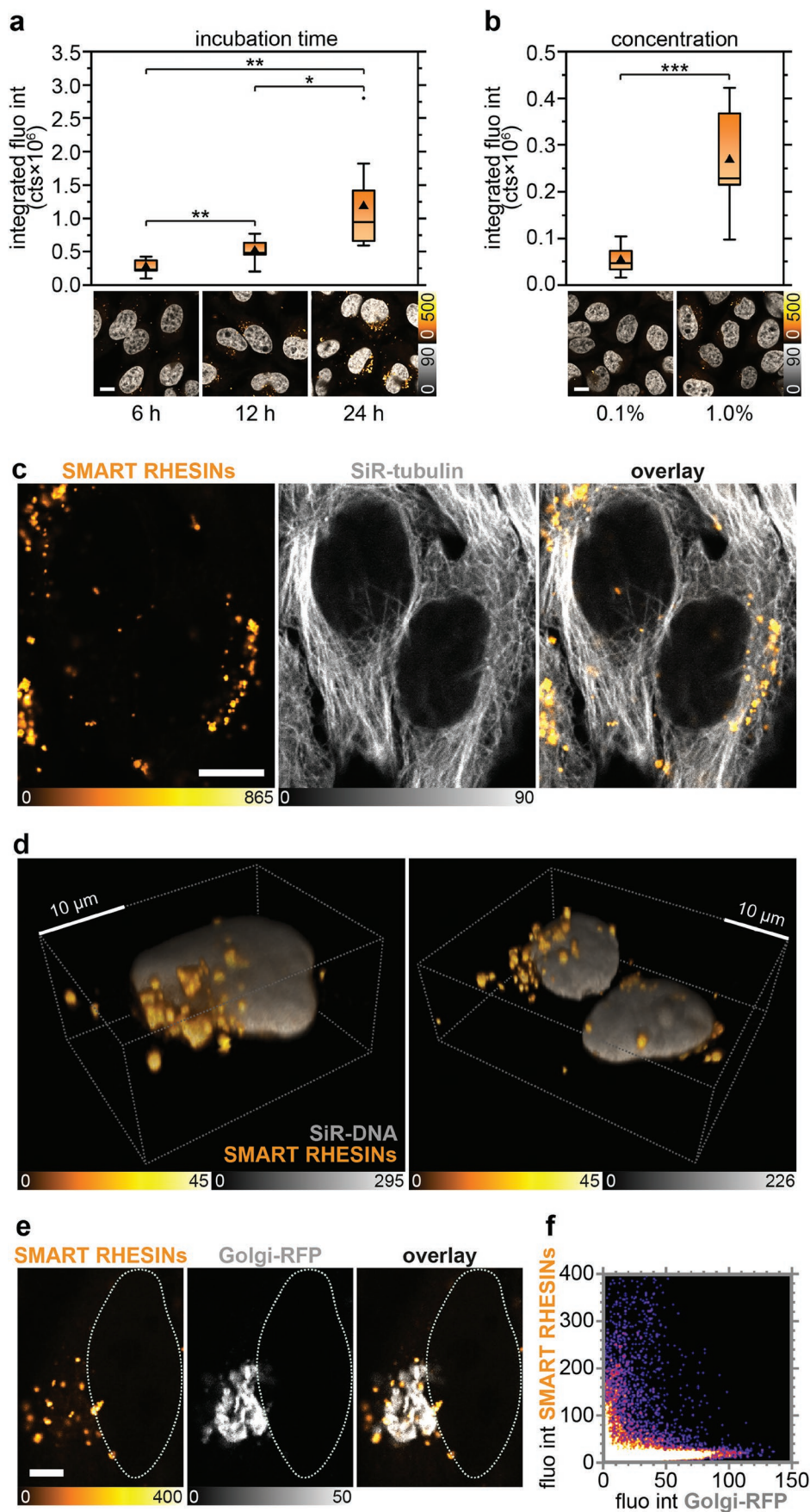
To assess if SMART RHESINs lose their luminescence properties over time, aliquots of SMART RHESINs were prepared in deionized H_2O and DMSO and the luminescence intensities were measured right after synthesis, after 1 week and

after 1 month. The aqueous aliquots showed a luminescence intensity decrease of $\approx 95\%$ over time, while the luminescence intensity of the DMSO aliquot stayed nearly constant with an intensity decrease of only 10% (Figures S5 and S6, Supporting Information). The quantum yields were determined in solution at room temperature, yielding values of $\Phi = 28\%$ for the native $[\text{Eu}(\text{TTA})_3(\text{H}_2\text{O})_2]$ complex, $\Phi = 32\%$ for Eu-TTA-Si, and $\Phi = 2\%$ for the SMART RHESINs. For better comparison, all samples were measured in ethanol absolute. The quantum yield of $[\text{Eu}(\text{TTA})_3(\text{H}_2\text{O})_2]$ is in good agreement with the literature.^[92] A decrease in the value for the SMART RHESINs could be explained by the many factors that affect luminescence quantum yields.^[93] These factors include temperature, solvent and the fact that SMART RHESINs were measured as a colloidal dispersion, which cannot avoid scattering effects.

Additionally, solid-state phosphorescence decay times were determined for $[\text{Eu}(\text{TTA})_3(\text{H}_2\text{O})_2]$ ($\tau = 0.05/0.22$ ms), Eu-TTA-Si ($\tau = 0.11/0.42$ ms), and SMART RHESINs ($\tau = 0.03/0.19/0.66$ ms), which exhibit double-exponential decay times in the range of tenths and hundredths of milliseconds due to their complex PL kinetics (Figure S7, Supporting Information). The decay times of the Eu(III) complexes that we measured are close to the range of 0.5–3 ms for lanthanides reported in the literature.^[67,94]

2.4. Confocal Imaging of SMART RHESINs

In live cell confocal fluorescence microscopy experiments, HeLa cells displayed distinct SMART RHESINs cytoplasmic luminescence signal increasing with nanosphere incubation time and concentration (Figure 5a,b), indicative of active cellular



uptake via non-specific endocytosis.^[95] The signal was confined to 200 nm (diffraction-limited) to 1 μm -sized cytoplasmic spots and larger aggregates mostly distributed heterogeneously around the nucleus, which always remained free of nanosphere signal (Figure 5c). To better map the intracellular distribution of SMART RHESINs over the entire cellular volume, confocal z-stacks of living HeLa cells co-stained with SiR-DNA were acquired. The data confirm the presence of cytoplasmic nanosphere accumulation hotspots in nuclear proximity (Figure 5d).

To analyze the intracellular fate of SMART RHESINs, colocalization experiments with commercial organelle stains against the Golgi apparatus (Golgi-RFP), lysosomes (SiR-lysosome), the endoplasmic reticulum (ER-RFP), and mitochondria (Mito-Tracker) were conducted. Calculation of the Pearson's correlation coefficient (PCC, pixel matching analysis)^[96] proved the absence of significant colocalization of SMART RHESINs with all of the co-stained organelles (PCC < 0.31, Figure S20, Supporting Information). However, visual inspection of the images revealed the distinct accumulation of SMART RHESINs in the region of the Golgi apparatus (Figure 5e,f, Figure S20b,f, Supporting Information), whereas any significant spatial correlation with lysosomes, ER and mitochondria was absent (Figure S20c–e,g–i, Supporting Information). Inspired by this intracellular fate, we speculate that the endocytosis of SMART RHESINs might be caveolae-dependent, as much cargo internalized via caveolae is eventually delivered to the Golgi apparatus.^[95] Further, we notice the application potential of our phenolic resin hollow sphere design as an organelle-targeted nano drug delivery system. Specifically directing drugs to the Golgi apparatus is highlighted as a promising strategy with high specificity, low-dose administration and reduced risk of side effects in therapy and diagnosis of cancer, neurological diseases and fibrosis.^[95] It has to be noted though that different cell types may employ different endocytotic pathways to internalize the same type of NP.^[97,98] Importantly, cancer cells internalize NPs with a higher efficiency than normal cells,^[99,100] which is encouraging for the potential application of SMART RHESINs as theranostic agents in the treatment of cancer. Although in vivo studies related to the biodistribution, biocompatibility, pharmacodynamics, pharmacokinetics, and enhanced permeability and retention effect (the EPR effect^[101,102]) of our SMART RHESINs are crucial factors to consider for its potential use in drug delivery for cancer therapy and diagnosis, these studies are beyond the scope of this paper and will require further research.

As the effective photostability of any luminescence reporter is crucial for the option of repeated and/or long-term readout under the experimental conditions of its actual application, we measured the photobleaching behavior of SMART RHESINs, $\text{Fe}_3\text{O}_4(\text{aq})@\text{PFRH}$ nanospheres, the silica-embedded complex

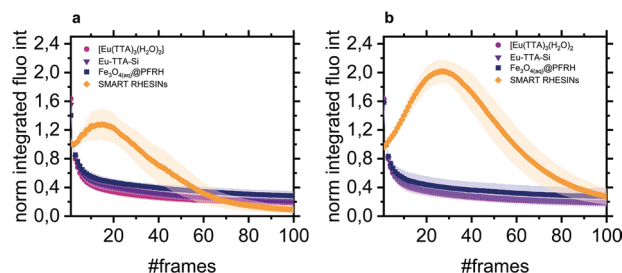


Figure 6. Photobleaching behavior studied by repeated confocal imaging of living HeLa cells incubated with 1% solutions of the native $[\text{Eu}(\text{TTA})_3(\text{H}_2\text{O})_2]$ complex (magenta circles), the silica-embedded complex Eu-TTA-Si (purple triangles), non-functionalized $\text{Fe}_3\text{O}_4(\text{aq})@\text{PFRH}$ nanospheres (dark blue squares), and SMART RHESINs (orange diamonds) for 18 h with all samples dispersed in a) DMSO and b) H_2O except for the native $[\text{Eu}(\text{TTA})_3(\text{H}_2\text{O})_2]$ complex because of its insoluble behavior in water. The integrated fluorescence intensity of $n = 20$ confocal fluorescence microscopy image series was normalized to the second frame. The means are plotted over the number of frames and the standard deviations are visualized as shadows.

Eu-TTA-Si, and the native $[\text{Eu}(\text{TTA})_3(\text{H}_2\text{O})_2]$ complex after their uptake into living HeLa cells by acquiring confocal image series of numerous fields of view and analyzing the integrated fluorescence intensity over the frame number. The experiments were performed for all samples with either DMSO (Figure 6a) or water (Figure 6b) stock solutions with an acquisition time of $0.64 \text{ frames s}^{-1}$.

Since the native $[\text{Eu}(\text{TTA})_3(\text{H}_2\text{O})_2]$ complex is insoluble in water, the complex's photobleaching measurements shown in Figure 6a,b were both performed with DMSO stock solutions. As shown in Figure 6, the fluorescence intensities of the native complex $[\text{Eu}(\text{TTA})_3(\text{H}_2\text{O})_2]$ and the silica-embedded complex Eu-TTA-Si decreased over time, as expected. In contrast, the SMART RHESINs showed an unexpected increase in fluorescence intensity for both the DMSO (Figure 6a) and water (Figure 6b) stock solutions, reaching a maximum after 20 and 30 frames, respectively, followed by an intensity decrease. In case of the DMSO stock solution, the fluorescence intensity of SMART RHESINs increased by about 20%, whereas, in the case of the water stock solution, it doubled compared to its initial value. To the end of the measurement, the normalized fluorescence intensities of all samples converge at around 20% of their initial values. However, the extent of fluorescence enhancement of SMART RHESINs upon repeated excitation depends on the solvent of the stock solution, which could indicate a solvent effect. Prior to the experiment, the DMSO or water stock solutions were diluted 1 to 100 in cell culture medium, that is,

Figure 5. Live cell confocal imaging of SMART RHESINs. a,b) Integrated SMART RHESINs fluorescence intensity after incubating living HeLa cells with a) 1.0% SMART RHESINs for 6, 12, and 24 h. b) 0.1% and 1.0% SMART RHESINs for 6 h ($n = 10$ cells), box plots indicate the interquartile range (box), the outer-most data points falling within 1.5 \times interquartile range (whiskers), the median (center line), and the mean (triangle). Bottom: exemplary confocal images with nuclear co-staining (SMART RHESINs orange; SiR-DNA gray). Scale bars, 10 μm . c) Confocal image of living HeLa cells after incubation with 1.0% SMART RHESINs (orange) for 24 h co-stained with SiR-tubulin (gray). Scale bar, 10 μm . d) Texture-based volume renderings of SMART RHESINs (1.0%, 24 h, orange) accumulation hotspots in proximity of the nucleus (co-stained with SiR-DNA, gray). e) Exemplary confocal image of the spatial correlation between SMART RHESINs (1.0%, 24 h, orange) and the Golgi apparatus (co-stained with CellLight Golgi-RFP BacMam 2.0) in a living HeLa cell. The outline of the nucleus is indicated with a dotted cyan line. Scale bar, 5 μm . f) Corresponding fluorogram (pixel matching analysis) of (e). Statistical significance (two-sided Student's t -test): ns—no significant difference, $*p < 0.05$, $**p < 0.005$, $***p < 0.0005$.

potential solvent effects could have already been manifested over time in the stock solution. During the actual measurement, the majority of the solvent is cell culture medium. The more pronounced fluorescence enhancement observed with the water stock solution samples could hint toward a gradual population of a solvent-induced long-lived dark state of the Eu-TTA-Si complex of the SMART RHESINs, which could be recovered by repeated excitation with 405 nm.

To investigate the special optical properties of the PFR polymer in more detail, ultraviolet-visible (UV-vis), PL, and PLE spectra of the Fe₃O₄@PFRH nanospheres without luminescence functionalization were measured at different excitation wavelengths (Figures S8 and S9, Supporting Information). At an excitation wavelength of 392 nm, the fluorescence emission of Fe₃O₄@PFRH shows two emission maxima, peaking at 455 and at 520 nm. PFR NPs are known to luminesce faintly green, which is interesting for microscopic applications and has previously been described in literature. For instance, PFR NPs emit at 511 nm when excited at 371 nm.^[103] PFR colloids have also been shown to emit luminescence between 490 and 520 nm, depending on their particle size.^[104] Fe₃O₄@PFR core/shell particles are reported to emit around 535 nm.^[105] The results shown in Figure 6 indicate that the population of the presumed dark state only occurs when the Eu-TTA-Si complex

and the PFRH polymer are present together in the form of the SMART RHESINs. The presumed dark state recovery is not observed with the individual components. As expected, their luminescence decreased with increasing illumination time.

2.5. Cytotoxicity of SMART RHESINs

To rigorously exclude potential acute cytotoxicity of SMART RHESINs, the frequency and duration of HeLa cell division (Figure 7a) were assessed by following cell proliferation via holographic time-lapse cytometry during constant nanosphere exposure for 48 h. Digital holographic microscopy allows for the non-invasive and label-free visualization of live cell populations by recording the light-wave-front information originating from the cells as a digital hologram and computationally processing it to produce a quantitative phase shift image (Figure S18a, Supporting Information). Additionally, the metabolic activity after nanosphere exposure was quantified by a cell viability assay based on the ability of viable cells to reduce the non-fluorescent redox dye resazurin to its fluorescent counterpart resorufin (Figure S18b, Supporting Information). As non-viable cells rapidly lose this metabolic capacity, the fluorescent signal is directly proportional to the number of living cells. We observed the

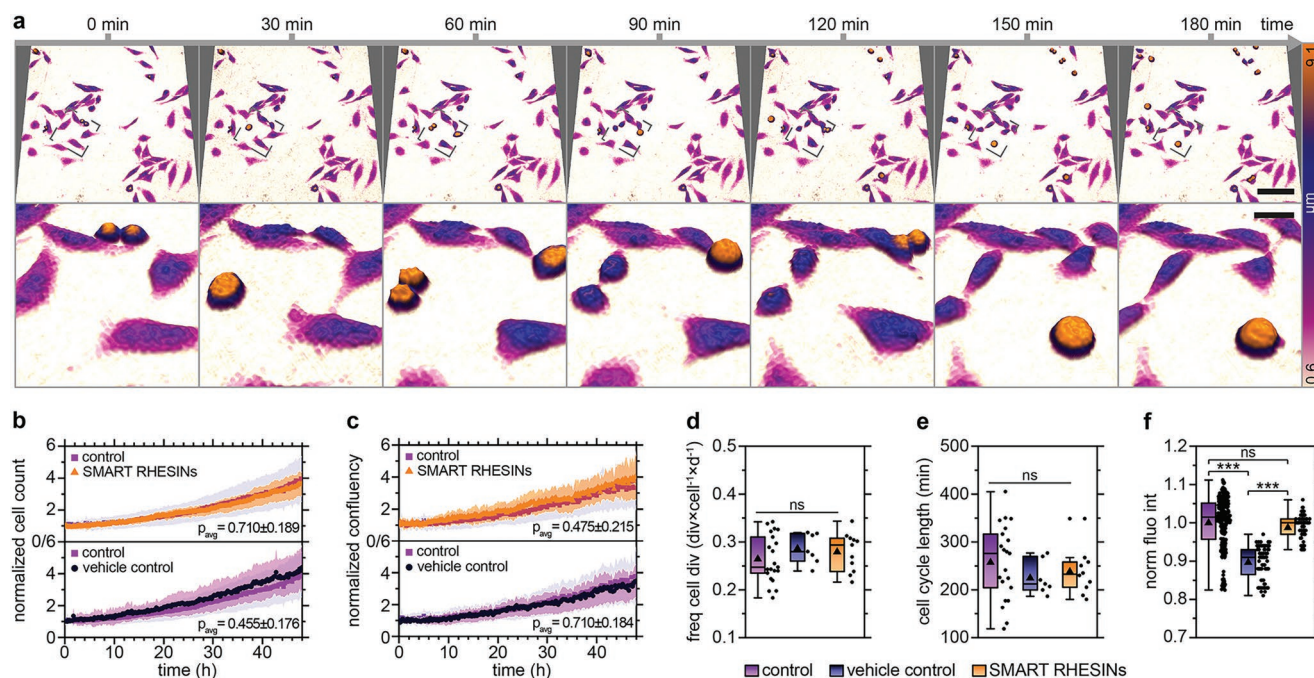


Figure 7. HeLa cell proliferation was followed for a total period of 48 h in the absence of (control, purple, experiments $n = 21$, tracked cells $n = 1182$, divisions $n = 311$, Movie S1, Supporting Information) and in the constant presence of 0.1% SMART RHESINs (orange, experiments $n = 11$, tracked cells $n = 1278$, divisions $n = 361$, Movie S2, Supporting Information) via holographic time-lapse cytometry. a) Holographic image sequence of several cell divisions in the presence of 0.1% SMART RHESINs (top: overview as shown in Movie S2, Supporting Information; bottom: zoom-in as marked in overview; $t = 0$ min equals $t = 28:45$ min in Movie S2, Supporting Information). Dividing cells round up and can be distinguished from non-dividing cells by height (color coded). Scale bar overview, 100 μm ; scale bar zoom-in, 20 μm . Corresponding time-lapse movie (Movie S2, Supporting Information) is supplied. b) Normalized cell count, c) normalized confluency, d) frequency of cell division of untreated (control), 0.1% DMSO treated (vehicle control), and 0.1% SMART RHESINs treated HeLa cells, and e) cell cycle length. f) CellTiter-Blue cell viability assay showing no influence of SMART RHESINs on metabolic activity of HeLa cells in comparison with control and vehicle control. For (b) and (c) the normalized means are plotted over the time and the standard deviations are visualized as shadows. For (d–f) box plots indicate the interquartile range (box), the outer-most data points falling within $1.5 \times$ interquartile range (whiskers), the median (center line), the mean (triangle), and the sample population (dots). Statistical significance (two-sided Student's t -test): ns—no significant difference to control, $*p < 0.05$, $**p < 0.005$, $***p < 0.0005$.

absence of acute cytotoxicity at SMART RHESINs working dilutions up to 1% as the cell morphology (Figure 7a, Figure S19a, Movies S1–S3, Supporting Information), cell proliferation rates (Figure 7b–e, Figure S19b–e, Supporting Information) and metabolic activity (Figure 7e, Figure S19f, Supporting Information) of living HeLa cells were not significantly affected over the time of the experiments. Indeed, the toxic concentrations were comparable to that of DMSO (vehicle). Note that potential long-term cytotoxic effects could not be assessed with the performed assays.

3. Conclusion

We have successfully synthesized europium(III)-coated hollow nanospheres filled with superparamagnetic magnetite NPs ($\text{Fe}_3\text{O}_4(\text{aq})@\text{PFRH}@Eu\text{-TTA-Si}$, SMART RHESINs). Our research revealed that the hollow nanosphere structure of these SMART RHESINs maintains the effective relaxation (Brownian plus Néel) even when immobilized. This unique behavior makes SMART RHESINs suitable for use in MPI and potentially allowing for the full exploitation of the quantitative nature of this technique in biological environments with significant change of the NP's mobility. These bimodal hollow nanospheres have a unique yolk/shell structure and the special optical properties of the combination of $[\text{Eu}(\text{TTA})_3(\text{H}_2\text{O})_2]$ and the PFR shell offer novel bioimaging opportunities. Our in vitro experiments highlight the extensive cellular tolerance and the favorable cellular fate, that is, the accumulation in the region of the Golgi apparatus, of SMART RHESINs, qualifying them as candidates for potential biomedical applications.

The chemical stability, superparamagnetism, exceptional luminescence, and absence of acute cytotoxicity of SMART RHESINs bode well for their application as multimodal imaging probes. Beyond in vitro applications for cell biology, combining the modalities of luminescence and magnetism within a NP provides pioneering opportunities for in vivo imaging. The design concept of SMART RHESINs matches the development of novel in vivo optical tomographic imaging techniques (e.g., MPI) that offer the prospect of a second imaging modality with higher spatial resolution and specificity. Our SMART RHESIN architecture is not restricted to the MNPs we synthesized and presented here, as the nanospheres can enclose various other types of MNPs. Therefore, it offers a versatile approach for utilizing established MPI-tracers or combining different types of MNPs, which is a key aspect of our ongoing research. We expect that these results will strongly motivate further development of multi-functionalized hollow nanospheres which could lead to significant advances in quantitative MPI techniques.

Supporting Information

Supporting Information is available from the Wiley Online Library or from the author.

Acknowledgements

This work was funded by the Deutsche Forschungsgemeinschaft (DFG, German Research Foundation, 363034336), supported by the

Baden-Württemberg Cooperative State University Karlsruhe Innovation Program Research (IPF) and a graduate scholarship granted by the State of Baden-Württemberg (Landesgraduiertenförderung for J.F.). The authors greatly acknowledge the support of the Karlsruhe Nano Micro Facility (KNMF, 2019-022-026870, 2020-024-029392) for the TEM measurements. For magnetic moment measurements, A.L.E. and Z.A.B. acknowledge J. M. Kikkawa and the University of Pennsylvania Property Measurement Facility, supported by MRSEC NSF DMR-1720530.

Open access funding enabled and organized by Projekt DEAL.

Conflict of Interest

Jochen Franke is employee of Bruker BioSpin MRI GmbH. All other authors declare no conflict of interest.

Data Availability Statement

The data that support the findings of this study are available in the supplementary material of this article.

Keywords

bimodal probes, europium-complex, hollow nanospheres, luminescence, magnetic particle imaging, magnetism, yolk/shell

Received: March 8, 2023

Revised: April 15, 2023

Published online:

- [1] B. Gleich (Philips Corporate Intellectual Property GmbH), German Patent *DE-10151778-A1*, 2001.
- [2] B. Gleich, J. Weizenecker, *Nature* **2005**, 435, 1214.
- [3] J. Sedlacik, A. Frölich, J. Spallek, N. D. Forkert, T. D. Faizy, F. Werner, T. Knopp, D. Krause, J. Fiehler, J.-H. Buhk, *PLoS One* **2016**, 11, e0160097.
- [4] A. Meola, J. Rao, N. Chaudhary, G. Song, X. Zheng, S. D. Chang, *World Neurosurg.* **2019**, 125, 261.
- [5] C. P. Bean, *J. Appl. Phys.* **1955**, 26, 1381.
- [6] R. M. Ferguson, A. P. Khandhar, S. J. Kemp, H. Arami, E. U. Saritas, L. R. Croft, J. Konkle, P. W. Goodwill, A. Halkola, J. Rahmer, *IEEE Trans. Med. Imaging* **2015**, 34, 1077.
- [7] a) B. Zheng, K. Lu, J. J. Konkle, D. W. Hensley, P. Keselman, R. D. Orendorff, Z. W. Tay, E. Yu, X. Y. Zhou, M. Bishop, B. Gunel, L. Taylor, R. M. Ferguson, A. P. Khandhar, S. J. Kemp, K. M. Krishnan, P. W. Goodwill, S. M. Conolly, in *Design and Applications of Nanoparticles in Biomedical Imaging*, (Eds: J. W. M. Bulte, M. M. J. Modo), Springer International Publishing, Cham **2017**, pp. 69–93; b) J. Franke, J. Chacon-Caldera, in *Magnetic Materials and Technologies for Medical Applications*, (Ed: A. M. Tishin), Woodhead Publishing, **2022**, pp. 339–393.
- [8] D. G. Mitchell, *J. Magn. Reson. Imaging* **1997**, 7, 1.
- [9] C. Lu, L. Han, J. Wang, J. Wan, G. Song, J. Rao, *Chem. Soc. Rev.* **2021**, 50, 8102.
- [10] K. Lu, P. W. Goodwill, E. U. Saritas, B. Zheng, S. M. Conolly, *IEEE Trans. Med. Imaging* **2013**, 32, 1565.
- [11] B. Yoo, Z. Medarova, in *Design and Applications of Nanoparticles in Biomedical Imaging*, (Eds: J. W. M. Bulte, M. M. J. Modo), Springer, Cham **2017**, pp. 171–186.

- [12] H. Paysen, N. Loewa, A. Stach, J. Wells, O. Kosch, S. Twamley, M. R. Makowski, T. Schaeffter, A. Ludwig, F. Wiekhorst, *Sci. Rep.* **2020**, *10*, 1922.
- [13] K. P. Melo, A. V. Makela, N. N. Knier, A. M. Hamilton, P. J. Foster, *Magn. Reson. Med.* **2022**, *87*, 312.
- [14] M. Utkur, E. U. Saritas, *Med. Phys.* **2022**, *49*, 2590.
- [15] S. A. Shah, D. B. Reeves, R. M. Ferguson, J. B. Weaver, K. M. Krishnan, *Phys. Rev. B: Condens. Matter Mater. Phys.* **2015**, *92*, 094438/1.
- [16] S. A. Corr, Y. P. Rakovich, Y. K. Gun'ko, *Nanoscale Res. Lett.* **2008**, *3*, 87.
- [17] S. Harvell-Smith, L. D. Tung, N. T. K. Thanh, *Nanoscale* **2022**, *14*, 3658.
- [18] H. T. K. Duong, A. Abdibastami, L. Gloag, L. Barrera, J. J. Gooding, R. D. Tilley, *Nanoscale* **2022**, *14*, 13890.
- [19] L. U. Khan, G. H. da Silva, A. M. Z. de Medeiros, Z. U. Khan, M. Gidlund, H. F. Brito, O. Moscoso-Londoño, D. Muraca, M. Knobel, C. A. Pérez, D. S. T. Martinez, *ACS Appl. Nano Mater.* **2019**, *2*, 3414.
- [20] A. Tufani, A. Qureshi, J. H. Niazi, *Mater. Sci. Eng., C* **2021**, *118*, 111545.
- [21] H. Terraschke, M. Franzreb, C. Wickleder, *Chem. - Eur. J.* **2020**, *26*, 6833.
- [22] R. Purbia, S. Paria, *Nanoscale* **2015**, *7*, 19789.
- [23] C. Chen, X. Fang, B. Wu, L. Huang, N. Zheng, *ChemCatChem* **2012**, *4*, 1578.
- [24] N. Rost, K. Sen, S. Savliwala, I. Singh, S. Liu, M. Unni, L. Raniero, C. Rinaldi, *J. Magn. Magn. Mater.* **2020**, *504*, 166675.
- [25] D. Zahn, J. Ackers, S. Dutz, T. Buzug, M. Graeser, *Int. J. Magn. Part. Imaging* **2022**, *8*, 1.
- [26] L. W. E. Starmans, D. Burdinski, N. P. M. Haex, R. P. M. Moonen, G. J. Strijkers, K. Nicolay, H. Grull, *PLoS One* **2013**, *8*, e57335.
- [27] K. Fang, L. Song, Z. Gu, F. Yang, Y. Zhang, N. Gu, *Colloids Surf., B* **2015**, *136*, 712.
- [28] M. C. Taira, N. S. Chiamoni, K. M. Pecuch, S. Alonso-Romanowski, *Drug Delivery* **2004**, *11*, 123.
- [29] M. I. Anik, M. K. Hossain, I. Hossain, A. M. U. B. Mahfuz, M. T. Rahman, I. Ahmed, *Nano Select* **2021**, *2*, 1146.
- [30] J. Park, K. An, Y. Hwang, J.-G. Park, H.-J. Noh, J.-Y. Kim, J.-H. Park, N.-M. Hwang, T. Hyeon, *Nat. Mater.* **2004**, *3*, 891.
- [31] D. Kim, N. Lee, M. Park, B. H. Kim, K. An, T. Hyeon, *J. Am. Chem. Soc.* **2009**, *131*, 454.
- [32] X. Zhang, L. Clime, H. Roberge, F. Normandin, L. H. Yahia, E. Sacher, T. Veres, *J. Phys. Chem. C* **2011**, *115*, 1436.
- [33] D. Chen, L. Li, F. Tang, S. Qi, *Adv. Mater.* **2009**, *21*, 3804.
- [34] a) Y.-K. Huang, C.-H. Su, J.-J. Chen, C.-T. Chang, Y.-H. Tsai, S.-F. Syu, T.-T. Tseng, C.-S. Yeh, *ACS Appl. Mater. Interfaces* **2016**, *8*, 14470; b) O. Buchholz, K. Sajjamar, J. Franke, H. Wei, A. Behrends, C. Munkel, C. Grüttner, D. von Elverfeldt, T. Buzug, S. Bär, *arXiv preprint arXiv:2304.06554* **2023**, 1.
- [35] G.-H. Wang, J. Hilgert, F. H. Richter, F. Wang, H.-J. Bongard, B. Spliethoff, C. Weidenthaler, F. Schüth, *Nat. Mater.* **2014**, *13*, 293.
- [36] L. H. Baekeland, *US Patent 942699*, **1909**.
- [37] R. Rego, P. J. Adriaenssens, R. A. Carleer, J. M. Gelan, *Polymer* **2004**, *45*, 33.
- [38] D.-S. Bin, Z.-X. Chi, Y. Li, K. Zhang, X. Yang, Y.-G. Sun, J.-Y. Piao, A.-M. Cao, L.-J. Wan, *J. Am. Chem. Soc.* **2017**, *139*, 13492.
- [39] T. Li, M. Cao, J. Liang, X. Xie, G. Du, *Polymers* **2017**, *9*, 426.
- [40] B. Patel, M. Patel, *J. Indian Chem. Soc.* **1988**, *65*, 651.
- [41] Q. Sun, C.-Z. Guo, G.-H. Wang, W.-C. Li, H.-J. Bongard, A.-H. Lu, *Chem. - Eur. J.* **2013**, *19*, 6217.
- [42] A.-H. Lu, W.-C. Li, G.-P. Hao, B. Spliethoff, H.-J. Bongard, B. B. Schaack, F. Schüth, *Angew. Chem., Int. Ed.* **2010**, *49*, 1615.
- [43] F. Al-Rimawi, A. Ahmad, F. I. Khalili, M. S. Mubarak, *Solvent Extr. Ion Exch.* **2004**, *22*, 721.
- [44] S. Wang, P. Yang, X. Sun, H. Xing, J. Shi, *J. Appl. Polym. Sci.* **2021**, *138*, 50416.
- [45] P. Yang, Y. Zhao, Y. Lu, Q.-Z. Xu, X.-W. Xu, L. Dong, S.-H. Yu, *ACS Nano* **2011**, *5*, 2147.
- [46] S. R. Guo, J. Y. Gong, P. Jiang, M. Wu, Y. Lu, S. H. Yu, *Adv. Funct. Mater.* **2008**, *18*, 872.
- [47] A. M. Derfus, W. C. W. Chan, S. N. Bhatia, *Nano Lett.* **2004**, *4*, 11.
- [48] N. Lamichhane, P. S. Shalini, A. K. Verma, I. Roy, T. Sen, *Biomedicines* **2021**, *9*, 288.
- [49] F. D. Heikham, D. S. Thiyam, *ChemistrySelect* **2017**, *2*, 10010.
- [50] Y.-S. Cho, T.-J. Yoon, E.-S. Jang, K. S. Hong, S. Y. Lee, O. R. Kim, C. Park, Y.-J. Kim, G.-C. Yi, K. Chang, *Cancer Lett.* **2010**, *299*, 63.
- [51] H.-S. Cho, Z. Dong, G. M. Pauletti, J. Zhang, H. Xu, H. Gu, L. Wang, R. C. Ewing, C. Huth, F. Wang, D. Shi, *ACS Nano* **2010**, *4*, 5398.
- [52] T. Sim, B. Choi, S. W. Kwon, K.-S. Kim, H. Choi, A. Ross, D.-H. Kim, *ACS Nano* **2021**, *15*, 12780.
- [53] A. V. S. Lourenço, C. A. Kodaira, E. M. Ramos-Sanchez, M. C. F. C. Felinto, H. Goto, M. Gidlund, O. L. Malta, H. F. Brito, *J. Inorg. Biochem.* **2013**, *123*, 11.
- [54] J. H. Monteiro, *Molecules* **2020**, *25*, 2089.
- [55] A. P. Demchenko, *Methods Appl. Fluoresc.* **2020**, *8*, 022001.
- [56] W. Gong, P. Das, S. Samanta, J. Xiong, W. Pan, Z. Gu, J. Zhang, J. Qu, Z. Yang, *Chem. Commun.* **2019**, *55*, 8695.
- [57] H. R. Chandan, J. D. Schiffman, R. G. Balakrishna, *Sens. Actuators, B* **2018**, *258*, 1191.
- [58] L.-J. Zhang, L. Xia, H.-Y. Xie, Z.-L. Zhang, D.-W. Pang, *Anal. Chem.* **2019**, *91*, 532.
- [59] P. T. Snee, *Acc. Chem. Res.* **2018**, *51*, 2949.
- [60] V. R. Mann, A. S. Powers, D. C. Tilley, J. T. Sack, B. E. Cohen, *ACS Nano* **2018**, *12*, 4469.
- [61] S. Probst, R. E. B. Kishen, D. C. Kluth, C. O. C. Bellamy, *PLoS One* **2016**, *11*, e0163856.
- [62] J. P. Simeunović, J. Pekárková, J. Žák, I. Chamradová, J. Hubálek, *Monatsh. Chem.* **2017**, *148*, 1901.
- [63] N. B. D. Lima, S. M. C. Gonçalves, S. A. Júnior, A. M. Simas, *Sci. Rep.* **2013**, *3*, 2395.
- [64] N. M. Cordina, N. Sayyadi, L. M. Parker, A. Everest-Dass, L. J. Brown, N. H. Packer, *Sci. Rep.* **2018**, *8*, 4521.
- [65] J. Trägårdh, G. Robb, R. Amor, W. B. Amos, J. Dempster, G. McConnell, *J. Microsc.* **2015**, *259*, 210.
- [66] E. Hemmer, A. Benayas, F. Légaré, F. Vetrone, *Nanoscale Horiz.* **2016**, *1*, 168.
- [67] G. Bao, S. Wen, G. Lin, J. Yuan, J. Lin, K.-L. Wong, J.-C. G. Bünzli, D. Jin, *Coord. Chem. Rev.* **2021**, *429*, 213642.
- [68] M. Yao, W. Chen, *Anal. Chem.* **2011**, *83*, 1879.
- [69] J. L. Kropp, M. W. Windsor, *J. Chem. Phys.* **1965**, *42*, 1599.
- [70] L. U. Khan, R. Petry, A. J. Paula, M. Knobel, D. S. T. Martinez, *Chem-NanoMat* **2018**, *4*, 1202.
- [71] X. Liu, P. Song, J. Hou, B. Wang, F. Xu, X. Zhang, *ACS Sustainable Chem. Eng.* **2018**, *6*, 2797.
- [72] G. Wang, W. Li, G. Shi, Y. Tian, L. Kong, N. Ding, J. Lei, Z. Jin, J. Tian, Y. Du, *Eur. J. Nucl. Med. Mol. Imaging* **2022**, *49*, 2723.
- [73] F. Ye, Á. Barrefelt, H. Asem, M. Abedi-Valuggerdi, I. El-Serafi, M. Saghafian, K. Abu-Salah, S. Alrokayan, M. Muhammed, M. Hassan, *Biomaterials* **2014**, *35*, 3885.
- [74] L. Chen, P. Jiang, X. Shen, J. Lyu, C. Liu, L. Li, Y. Huang, *Small* **2022**, *19*, 2204747.
- [75] S. K. Movahed, N. F. Lehi, M. Dabiri, *J. Catal.* **2018**, *364*, 69.
- [76] M. Priebe, K. M. Fromm, *Chem. - Eur. J.* **2015**, *21*, 3854.
- [77] L. Yu, X. Y. Yu, X. W. Lou, *Adv. Mater.* **2018**, *30*, 1800939.
- [78] M. Zhu, Y. Cheng, Q. Luo, M. El-khateeb, Q. Zhang, *Mater. Chem. Front.* **2021**, *5*, 2552.
- [79] A. V. Makela, J. M. Gaudet, D. H. Murrell, J. R. Mansfield, M. Wintermark, C. H. Contag, *Neuroscience* **2021**, *474*, 100.
- [80] A. H. Yusoff, M. N. Salimi, M. F. Jamlos, *Adv. Nano Res.* **2018**, *6*, 1.
- [81] A. Ali, H. Zafar, M. Zia, I. ul Haq, A. R. Phull, J. S. Ali, A. Hussain, *Nanotechnol., Sci. Appl.* **2016**, *9*, 49.

- [82] E. Scopel, P. P. Conti, D. G. Stroppa, C. J. Dalmaschio, *SN Appl. Sci.* **2019**, *1*, 147.
- [83] S. Munjal, N. Khare, *J. Nanopart. Res.* **2017**, *19*, 18.
- [84] M. Lattuada, T. A. Hatton, *Langmuir* **2007**, *23*, 2158.
- [85] Y. E. Jad, G. A. Acosta, S. N. Khattab, B. G. de la Torre, T. Govender, H. G. Kruger, A. El-Faham, F. Albericio, *Org. Biomol. Chem.* **2015**, *13*, 2393.
- [86] M. Fleet, *Acta Crystallogr.* **1981**, *B37*, 917.
- [87] M. E. F. Brollo, S. Veintemillas-Verdaguer, C. M. Salván, M. d. P. Morales, *Contrast Media Mol. Imaging* **2017**, *2017*, 8902424.
- [88] R. P. Araújo-Neto, E. L. Silva-Freitas, J. F. Carvalho, T. R. F. Pontes, K. L. Silva, I. H. M. Damasceno, E. S. T. Egito, A. L. Dantas, M. A. Morales, A. S. Carriço, *J. Magn. Magn. Mater.* **2014**, *364*, 72.
- [89] M. M. Nolasco, P. M. Vaz, V. T. Freitas, P. P. Lima, P. S. André, R. A. S. Ferreira, P. D. Vaz, P. Ribeiro-Claro, L. D. Carlos, *J. Mater. Chem. A* **2013**, *1*, 7339.
- [90] a) C. P. Bean, I. S. Jacobs, *J. Appl. Phys.* **1956**, *27*, 1448; b) C. P. Bean, J. D. Livingston, *J. Appl. Phys.* **1959**, *30*, 1205.
- [91] O. Kosch, H. Paysen, J. Wells, F. Ptach, J. Franke, L. Wöckel, S. Dutz, F. Wiekhorst, *J. Magn. Magn. Mater.* **2019**, *471*, 444.
- [92] M. Fernandes, V. de Zea Bermudez, R. A. Sá Ferreira, L. D. Carlos, N. V. Martins, *J. Lumin.* **2008**, *128*, 205.
- [93] M. A. Omary, H. H. Patterson, in *Encyclopedia of Spectroscopy and Spectrometry (Third Edition)*, (Eds: J. C. Lindon, G. E. Tranter, D. W. Koppenaal), Academic Press, Oxford **2017**, pp. 636–653.
- [94] J. R. Lakowicz, *Principles of Fluorescence Spectroscopy*, Springer Science+Business Media, LLC, New York, **2008**.
- [95] S. Behzadi, V. Serpooshan, W. Tao, M. A. Hamaly, M. Y. Alkawareek, E. C. Dreaden, D. Brown, A. M. Alkilany, O. C. Farokhzad, M. Mahmoudi, *Chem. Soc. Rev.* **2017**, *46*, 4218.
- [96] K. W. Dunn, M. M. Kamocka, J. H. McDonald, *Am. J. Physiol. Cell Physiol.* **2011**, *300*, C723.
- [97] T. Xia, M. Kovochich, M. Liong, J. I. Zink, A. E. Nel, *ACS Nano* **2008**, *2*, 85.
- [98] T. dos Santos, J. Varela, I. Lynch, A. Salvati, K. A. Dawson, *PLoS One* **2011**, *6*, e24438.
- [99] K. Bromma, A. Bannister, A. Kowalewski, L. Cicon, D. B. Chithrani, *Cancer Nanotechnol.* **2020**, *11*, 8.
- [100] E. C. Costa, V. M. Gaspar, J. G. Marques, P. Coutinho, I. J. Correia, *PLoS One* **2013**, *8*, e70072.
- [101] Y. Matsumura, H. Maeda, *Cancer Res.* **1986**, *46*, 6387.
- [102] M. A. Subhan, Y. S. S. Kishan, N. Filipczak, F. Parveen, V. P. Torchilin, *J. Pers. Med.* **2021**, *11*, 571.
- [103] Z. F. Gao, A. Y. Ogbe, E. E. Sann, X. Wang, F. Xia, *Talanta* **2018**, *180*, 12.
- [104] J. Zhang, Y. Yuan, Z.-L. Yu, A. Yu, S.-H. Yu, *Small* **2014**, *10*, 3662.
- [105] P. Yang, Q. Z. Xu, S. Y. Jin, Y. Zhao, Y. Lu, X. W. Xu, S. H. Yu, *Chem. - Eur. J.* **2012**, *18*, 1154.